Journal of Power Sources 230 (2013) 50–58

Contents lists available at SciVerse ScienceDirect

Journal of Power Sources

journal homepage: www.elsevier.com/locate/jpowsour

Nitrogen-doped porous carbon for supercapacitor with long-term electrochemical stability

Xiang Ying Chen [a,*], Chong Chen [a], Zhong Jie Zhang [b], Dong Hua Xie [a], Xiao Deng [a], Jian Wei Liu [c,**]

[a] School of Chemical Engineering, Anhui Key Laboratory of Controllable Chemistry Reaction & Material Chemical Engineering, Hefei University of Technology, Hefei, Tunxi Road 193#, Anhui 230009, PR China
[b] College of Chemistry & Chemical Engineering, Anhui Province Key Laboratory of Environment-Friendly Polymer Materials, Anhui University, Hefei 230039, Anhui, PR China
[c] Department of Physics and Astronomy, University of Kansas, Lawrence, KS 66045, United States

HIGHLIGHTS

- A direct carbonization method was developed to prepare porous carbon.
- UF resins can not only serve as carbon source but also as nitrogen source.
- The surface areas and pore structures of porous carbon can be simply tuned.
- The carbon sample exhibits excellent long-term electrochemical stability.

ARTICLE INFO

Article history:
Received 31 October 2012
Received in revised form
3 December 2012
Accepted 14 December 2012
Available online 22 December 2012

Keywords:
Urea formaldehyde resins
$Ca(OAc)_2$
Template
Supercapacitor

ABSTRACT

Nitrogen-doped porous carbons have been prepared by a direct carbonization of the mixture of urea formaldehyde resins (*abbr.* UF resins) and calcium acetate monohydrate. The experimental results reveal that the mass ratios of UF resins-to-$Ca(OAc)_2 \cdot H_2O$ and carbonization temperatures can play crucial roles in the formation of porous carbon with various surface area and structure as well as determining the carbons' surface areas, pore structures and capacitive performance. The **UF-Ca-700-3:1** sample exhibits much large specific capacitances *ca.* 334.8 F g^{-1} and 224.0 F g^{-1} at the current density of 0.5 and 1.0 A g^{-1} in 6.0 mol L^{-1} aqueous KOH aqueous electrolyte, respectively. The **UF-Ca-900-3:1** displays more superior rate capability, which can possess high specific capacitance retention as *ca.* 67.1% and 51.4% at the high current densities of 20 and 40 A g^{-1}, respectively. In addition, a capacity fading lower than 1% after 5000 cycles of charging and discharging is obtained, indicating its long-term electrochemical stability.

1. Introduction

Carbon materials, such as activated carbons, carbon nanotubes and graphene have attracted very broad attention due to low cost, variety of form (powders, fibers, aerogels, composites, sheets, monoliths, tubes *etc.*), ease of processability, inert electrochemistry and controllable porosity [1,2]. Consequently, carbon electrodes have been extensively applied in supercapacitor devices, commonly exhibiting long durability, high specific power (more than 10 kW kg^{-1}) and high dynamic of charge propagation, which can bridge the gap between batteries and dielectric capacitors [3–5]. Among them, porous carbons are particular interest because of their high surface area, tunable pore size and distribution [6,7]. Various methods were proposed to prepare porous carbons with adjustable pore structures. Knox et al. developed a template method for the synthesis of porous carbons [8]. The template method can be classified into soft template and hard template. Soft templates are thermally unstable organic molecules, which can be removed by calcining the starting framework, accompanied with the formation of porous carbons. Hard templates, possessing inherited porosity, are usually infiltrated with carbon precursor, followed by carbonization and etching of the template using NaOH or HF solution. As a result, porous carbons appear with the pore size and structure being an inverse replica of that from the original template [9–11]. So far, several kinds of impressive hard templates for preparing porous carbons have been proposed, including silica [12], zeolite [13], MgO [14], $Mg(OH)_2$ [15], anodized aluminum oxide (AAO) [16].

Urea formaldehyde resins (*abbr.* UF resins), also known as urea-methanal, is a non-transparent thermosetting resin or plastic, made

* Corresponding author. Tel./fax: +86 551 2901450.
** Corresponding author. Tel.: +1 785 8642274; fax: +1 785 8645264.
E-mail addresses: cxyhfut@gmail.com (X.Y. Chen), zhangzj0603@126.com (Z.J. Zhang), liuw@ku.edu (J.W. Liu).

0378-7753/$ – see front matter © 2012 Elsevier B.V. All rights reserved.
http://dx.doi.org/10.1016/j.jpowsour.2012.12.054

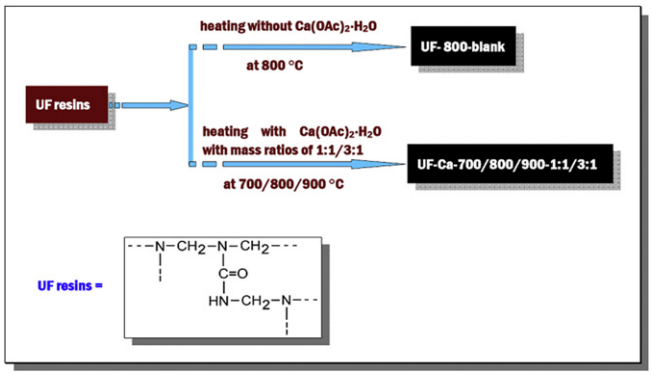

Fig. 1. Schematic routes showing the production of porous carbon by heating UF resins and $Ca(OAc)_2 \cdot H_2O$ with mass ratios of 1:1 and 3:1 at carbonization temperatures of 700, 800 and 900 °C, in which $Ca(OAc)_2 \cdot H_2O$ serves as hard template.

from urea and formaldehyde heated in the presence of a mild base such as ammonia or pyridine. These resins are used in adhesives, finishes, medium density fiberboard (MDF), and molded objects. Taking into accounts the composition of UF resins, the carbons derived from UF resins especially with high content of nitrogen in carbon matrix are expected to display excellent capacitive performance because nitrogen dopant can cause a shift of the Fermi level to the valence band in carbon electrode, thereby facilitating the electron transfer [17]. The precursor can be used as a starting material for the fabrication of nitrogen-doped porous carbon.

Here, we report a template synthetic method to prepare nitrogen-doped porous carbons by the direct carbonization of the mixture of UF resins and calcium acetate monohydrate ($Ca(OAc)_2 \cdot H_2O$) without further chemical/physical activation process, hereinto calcium acetate monohydrate acts as hard template. We found that the mass ratios of UF resins-to-$Ca(OAc)_2 \cdot H_2O$ and carbonization temperatures affect the surface area and morphologies of porous carbon. The nitrogen-doped porous carbon can be directly used as supercapacitor electrodes. A remarkable specific capacitance of 334.8 F g^{-1} has been obtained using **UF-Ca-700-3:1** sample. Moreover, the improved cycle stability (a capacity fading lower than 1% with 5000 cycles) can be achieved toward the **UF-Ca-900-3:1** sample.

2. Experimental

All the chemicals were purchased from Sinopharm Chemical Reagent (Shanghai) Co. Ltd with analytical grade, and were used as received without further treatment.

In a typical experiment, the UF resins were first heated at 800 °C for 2 h under Ar flow to obtain **UF-800-blank**. In order to investigate the effect of calcium acetate monohydrate on the formation of pore structures within carbons, UF resins and $Ca(OAc)_2 \cdot H_2O$ with mass ratios of 1:1 and 3:1 were heated together at the carbonization temperatures of 700/800/900 °C for 2 h under Ar flow. The resulting products were named as **UF-Ca-700/800/900-1:1/3:1**. The schematic routes and the unit structure of UF resin are depicted in Fig. 1.

2.1. Typical synthetic procedure for UF-Ca-900-3:1 sample

UF resins and $Ca(OAc)_2 \cdot H_2O$ powder with the mass ratio of 3:1 were first ground, and then placed in a porcelain boat, flushing with Ar flow for 30 min, and further heated in a horizontal tube furnace up to 900 °C at a rate of 5 °C min^{-1} and maintained at 900 °C for 2 h under Ar flow. The resultant product was immersed with dilute HCl solution to remove soluble/insoluble substances, subsequently washed with adequate deionized water until pH = 7. Finally, the sample was dried under vacuum at 120 °C for 12 h to obtain the **UF-Ca-900-3:1** sample.

2.2. Characterization

X-ray diffraction (XRD) patterns were obtained on a Rigaku D/MAX2500V with Cu Kα radiation. Field emission scanning electron microscopy (FESEM) images were taken with a Hitachi S-4800 scanning electron microscope. X-ray photoelectron spectra (XPS) were obtained on a VG ESCALAB MK II X-ray photoelectron spectrometer with an exciting source of Mg Kα (1253.6 eV). The specific surface area and pore structure of the carbon samples were determined by N_2 adsorption-desorption isotherms at 77 K (Micrometrics ASAP 2020 system) after being vacuum-dried at 200 °C overnight. The specific surface area was calculated by the conventional BET (Brunauer-Emmett-Teller) method. The pore size distribution (PSD) plot was recorded from the adsorption branch of the isotherm based on the Barrett–Joyner–Halenda (BJH) model.

2.3. Electrochemical measurements

In order to evaluate the capacitive performances of the as-prepared carbon samples (~4 mg) in electrochemical capacitors, a mixture of 80 wt% the carbon sample, 15 wt% acetylene black and

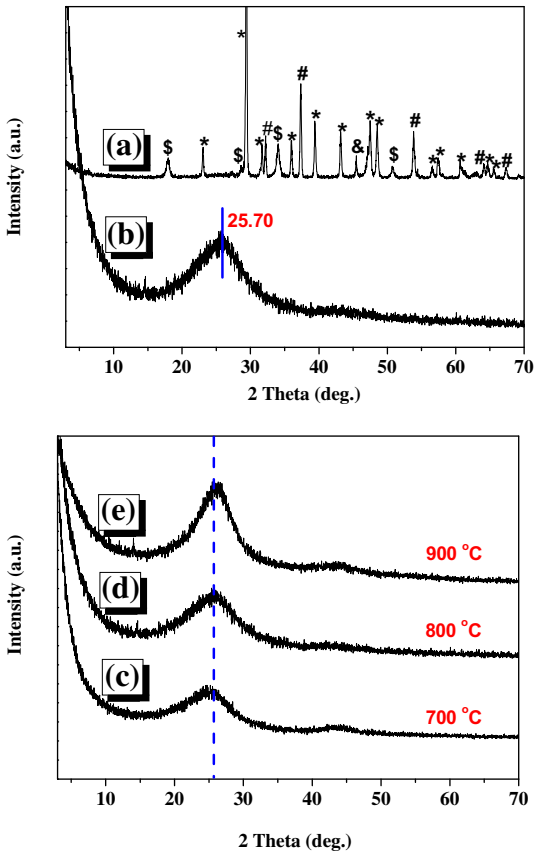

Fig. 2. XRD patterns of the **UF-Ca-800-3:1** sample before (a) and after (b) being washed with aqueous HCl solution and deionized water to remove any unwanted impurities; as well as the contrast XRD patterns of the (c) **UF-Ca-700-3:1**, (d) **UF-Ca-800-3:1** and (e) **UF-Ca-900-3:1** samples. Notes: * = hexagonal $CaCO_3$ (JCPDS card no. 47-1743); & = orthorhombic $CaCO_3$ (JCPDS card no. 71-2396); # = cubic CaO (JCPDS card no. 37-1497); $ = hexagonal $Ca(OH)_2$ (JCPDS card no. 04-0733).

5 wt% polytetrafluoroethylene (PTFE) binder was fabricated using ethanol as a solvent. Slurry of the above mixture was subsequently pressed onto nickel foam under a pressure of 20 MPa, serving as the current collector. The prepared electrode was placed in a vacuum drying oven at 120 °C for 24 h. A three electrode experimental setup taking a 6.0 mol L^{-1} KOH aqueous solution as electrolyte was used in cyclic voltammetry and galvanostatic charge–discharge measurements on an electrochemical working station (CHI660D, ChenHua Instruments Co. Ltd., Shanghai). Here, the prepared electrode, platinum foil (6 cm^2) and saturated calomel electrode (SCE) were used as the working, counter and reference electrodes, respectively. The whole electrochemical measurements were carried out at ~25 °C.

3. Results and discussion

The component, crystallinity and purity of the as-prepared samples were studied by XRD technique. Upon directly heating UF resins and $Ca(OAc)_2 \cdot H_2O$ with mass ratio of 3:1 at carbonization temperatures of 900 °C, lots of darkish product engendered and its powder XRD pattern is given in Fig. 2a, indicating its component of $CaCO_3$, CaO and $Ca(OH)_2$. According to the TGA-DTA analysis in the temperature range of 20–1000 °C [18,19], the thermal decomposition of $Ca(OAc)_2 \cdot H_2O$ can be primarily divided into three stages. At the temperature range of 180–220 °C, $Ca(OAc)_2 \cdot H_2O$ can lose H_2O molecule to form anhydrous $Ca(OAc)_2$, which further decompose to acetone and $CaCO_3$ at 340–480 °C. Following this, $CaCO_3$ will decompose to form CaO and CO_2 beyond the temperature of 803 °C. Therefore, in present work, CaO is the decomposition product of $CaCO_3$ derived from $Ca(OAc)_2$ while the formation of $Ca(OH)_2$ is incurred by the deliquescence of CaO. The existence of $CaCO_3$ in the products can also be evidenced by the appearance of massive bubbles when introducing aqueous HCl solution. Besides, the *in situ* formed CaO and/or $CaCO_3$ can act as hard templates for the formation of porous carbon structures, whereas the CO_2 gas from the decomposition of $CaCO_3$ might somewhat react with carbon sample as an activation agent.

After being washed with aqueous HCl solution and deionized water to remove any unwanted impurities, broad and low-intensity carbon diffraction peak centering at 25.70° (2θ value, correlative with Bragg Equation: $2d\sin\theta = \lambda$) appears, as shown in Fig. 2b. Compared with the standard 2θ value for hexagonal graphite (26.23–26.38°), the present one (25.70°) shift to lower direction with obvious augmentation of interplanar spacings of (002) plane, authentically revealing the amorphous nature or low degree of crystallinity. On the other hand, to investigate the impact of carbonization temperature upon the crystallinity of carbons, contrast experiments were carried out at 700, 800 and 900 °C, respectively. It is seen in Fig. 2c–e that three diffraction peaks are basically the same in shape. However, by careful observation upon (002) plane, we can discern that the 2θ values gradually shift to higher direction toward **UF-Ca-700-3:1**, **UF-Ca-800-3:1** and **UF-Ca-900-3:1** samples. In the light of Bragg Equation, it is thus concluded that higher carbonization temperature can favor for the enhancement of crystallinity of carbons.

The shapes and sizes of the carbon samples prepared by heating UF resins with/without $Ca(OAc)_2 \cdot H_2O$ at various carbonization temperatures of 700–900 °C were investigated by FESEM technique. Markedly, when heating the precursors at elevated temperatures especially beyond 300 °C, large quantity of black smoke emerges out of the tubular furnace, which are probably beneficial to the formation of porous structures within carbon materials. This phenomenon is to some extent consistent with the TGA result toward UF resins, in which predominate mass loss

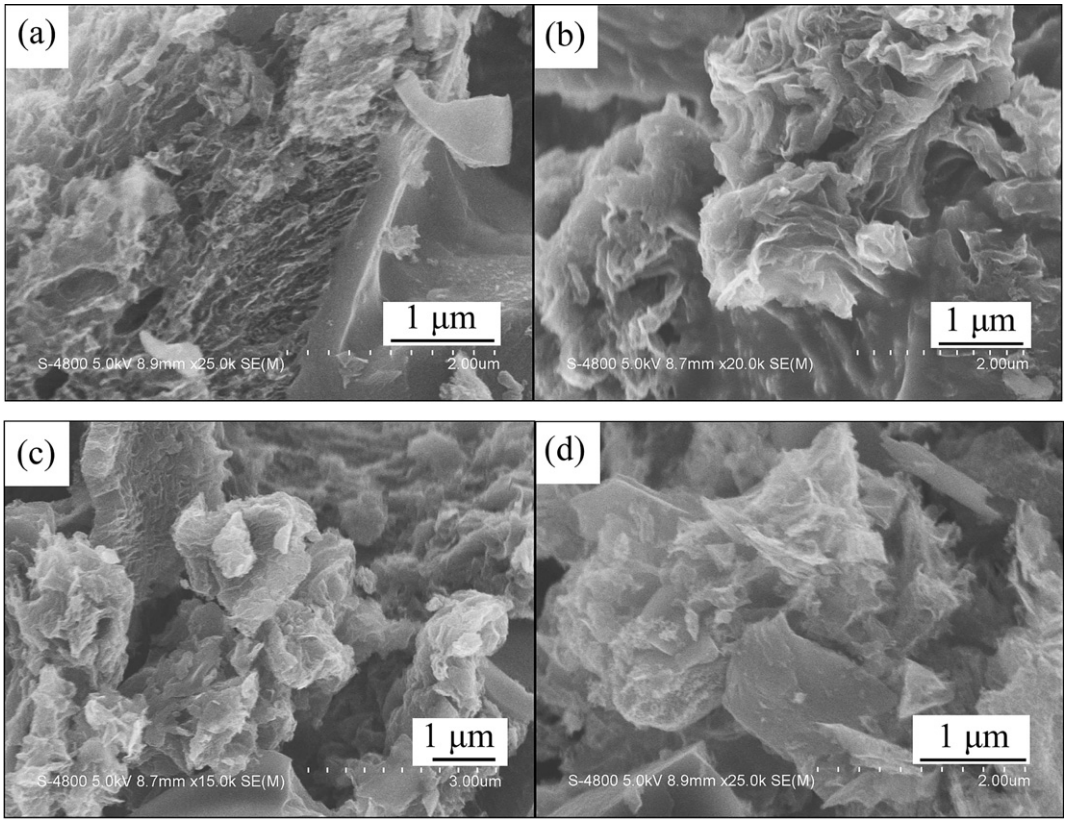

Fig. 3. FESEM images of the (a) **UF-800-blank**, (b) **UF-Ca-700-3:1**, (c) **UF-Ca-800-3:1** and (d) **UF-Ca-900-3:1** samples.

occurs at the carbonization temperatures of 250–400 °C [20]. Fig. 3a shows the representative FESEM image of **UF-800-blank**, which takes on irregular shapes with sizes of several micrometers and especially some parts possess porous structures by careful observation. Besides, the **UF-Ca-700-3:1**, **UF-Ca-800-3:1** and **UF-Ca-900-3:1** samples all consist of large numbers of irregular block particles of several micrometers in sizes with large-scale cavities covering on their surfaces, as displayed in Fig. 3b–d. With respect to the micro/meso-pores existing in these particles, they will be further detected by the following N_2 adsorption/desorption analysis.

The empirical composition, chemical state and electronic state of the elements existing within the present carbon samples were quantitatively determined by XPS technique. Taking into account the unit structure of UF resins depicted in Fig. 1, high nitrogen contents are expected to appear in the carbon products. As a result, this speculation was approved by the survey spectra (0–1400 eV) of the **UF-Ca-700-3:1**, **UF-Ca-800-3:1** and **UF-Ca-900-3:1** samples, as shown in Fig. 4a. All these carbon samples are basically composed of C, N and O elements without any other obvious impurities. Furthermore, considering the intensity discrepancies of elements in Fig. 4a, diverse contents especially the case of N 1s must occur in the products, mainly incurred by the different carbonization temperatures.

Fig. 4b demonstrates the asymmetric C 1s spectra ranging from 280.0 to 297.5 eV of the **UF-Ca-700-3:1**, **UF-Ca-800-3:1** and **UF-Ca-900-3:1** samples, which can be primarily fitted as three peaks centering at *ca.* 284.6, 285.8 and 287.8 eV, respectively. In details, the peak at *ca.* 284.6 eV proves the graphitic carbon, corresponding to the energy of the sp^2 C=C bond in C1s spectrum of pyrolytic graphite. The peak at *ca.* 285.8 eV can be assigned as sp^3 C–C/C–H bonds while the one *ca.* 287.8 eV attributes to –C=O/N–C=N bonds [21,22]. On the other hand, four nitrogen species commonly exist in nitrogen-containing carbon, including pyridinic nitrogen (398.6 ± 0.3 eV), pyrrolic nitrogen (400.5 ± 0.3 eV), graphitic nitrogen (also as quarternary nitrogen, 401.3 ± 0.3 eV), oxided pyridinic nitrogen (402–405 eV) [23–25]. Fig. 4b shows the asymmetric N 1s spectra ranging from 392.0 to 408.0 eV of the **UF-Ca-700-3:1**, **UF-Ca-800-3:1** and **UF-Ca-900-3:1** samples. All the N 1s spectra can be approximately divided into three peaks centering at *ca.* 398.4, 399.8 and 400.8 eV, corresponding to pyridinic nitrogen, pyrrolic nitrogen and graphitic nitrogen, respectively. Finally, the total XPS peak analyses of the carbon samples were summarized in Table 1. Apparently, along with the enhancement of carbonization temperature from 700 to 900 °C, the carbon content increases while the nitrogen and oxygen contents decrease, especially the pronounced change in case of 900 °C. This is probably induced by the volatilization of nitrogen/oxygen species at elevated carbonization temperature.

The specific surface areas and pore structures of the carbon samples were measured by N_2 adsorption-desorption technique at 77 K. Fig. 5a shows the typical hysteresis loops with sharp capillary condensation steps ($P/P_0 > 0.45$) toward the **UF-Ca-700-3:1**, **UF-Ca-800-3:1** and **UF-Ca-900-3:1** samples. All hysteresis loops correspond to type-IV according to the IUPAC classification, basically demonstrating their mesoporous structures with strong affinities

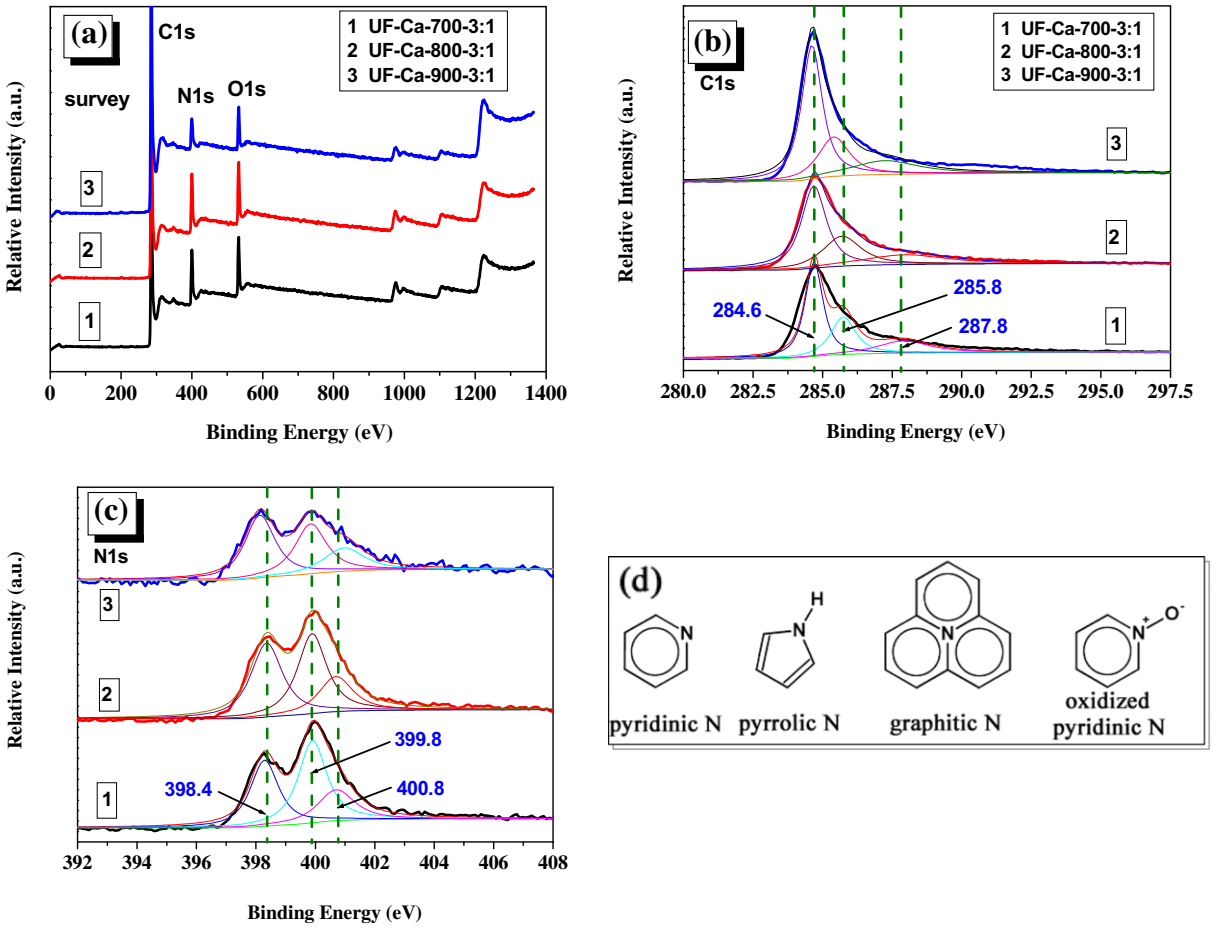

Fig. 4. XPS spectra of the carbon samples: (a) survey, (b) C1s and (c) N1s. Four types of nitrogen species commonly reported in nitrogen-doped carbon materials (d).

Table 1
XPS peak analysis of the carbon samples.

Sample	C (at. %)	N (at. %)	O (at. %)
UF-Ca-700-3:1	77.01	14.12	9.87
UF-Ca-800-3:1	76.84	13.68	9.48
UF-Ca-900-3:1	87.91	5.05	7.04

[26]. Besides, on the basis of the modern classification of hysteresis loops, the hysteresis loops in Fig. 5a can be assigned to type H-3, which does not exhibit any limiting adsorption at high P/P_o. It is believed that this type of isotherm occurs with aggregates of plate-like particles giving rise to slit-shaped pores [27]. Furthermore, the relative pressure ranges corresponding to capillary condensation become much wider in shape when increasing the carbonization temperatures from 700 to 900 °C, probably revealing the occurrence of pore propagation and pore-widening on the channel-like mesopores [28]. Fig. 5b shows the pore size distribution curves recorded from the adsorption branch of the isotherm based on BJH model, obviously proving their multi-modal pore structures. The coexistence of micro/meso/macro-scale pores in present work are believed to be ideal for supercapacitor, due to the actual energy storage occurring predominately in the smaller micropores while the larger pores provide fast mass-transport of electrolytes to and from the micropores [5,29].

On the other hand, as revealed in Table 2, the carbonization temperature plays a vital role in determining the BET surface area

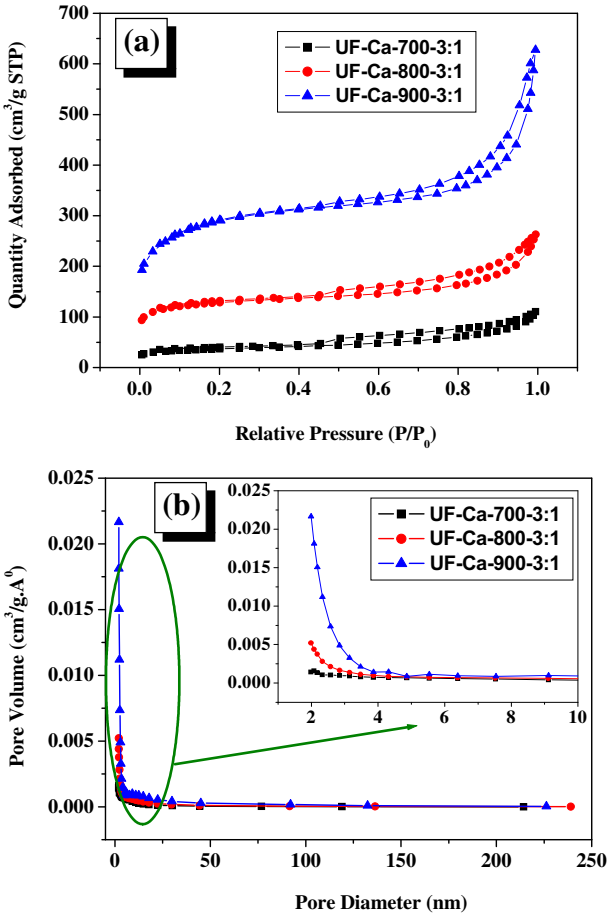

Fig. 5. N_2 adsorption/desorption isotherms and pore size distribution curves of the carbon samples.

(S_{BET}) and total pore volume (V_T) of the carbons. In case of S_{BET} value, the **UF-Ca-800-3:1** and **UF-Ca-900-3:1** samples have increased up to *ca.* 249.2% and 688.3%, respectively, in contrast to that of the **UF-Ca-700-3:1** sample. The V_T values of **UF-Ca-800-3:1** and **UF-Ca-900-3:1** samples have respectively increased up to *ca.* 150.0% and 464.3%, compared with that of the **UF-Ca-700-3:1** sample. Besides, the micropore area and external surface area values are nearly equal, as listed in Table 2, incredibly indicating that the contributions from micropore and larger pores (meso-/macropores) are approximately identical.

The electrochemical behaviors were examined by cyclic voltammetry (CV) technique performed in a potential range of −1.0–0 V. Fig. 6 shows the CV curves of the **UF-Ca-700-3:1**, **UF-Ca-800-3:1** and (d) **UF-Ca-900-3:1** samples at the scan rates of 20/50/100/200 mV s^{-1}. In case of 20 mV s^{-1}, as given in Fig. 6a, the **UF-Ca-900-3:1** sample exhibits an almost ideally rectangular shape, showing almost mirror images with respect to the zero-current line, which is characteristic of an electric double-layer capacitor (EDLC) [30]. However, the CV curves toward **UF-Ca-700-3:1** and **UF-Ca-800-3:1** greatly deviate from rectangular shape, probably incurred by higher contents of oxygen-containing functional groups on the surfaces of the electrodes [31], which to some extent accords with the XPS values shown in Table 1. Besides, all the CV curves in Fig. 6a possess no obvious oxidation/reduction peaks, revealing no pseudo-capacitance involved or very little contribution from redox reaction. Furthermore, according to the integral areas surrounded by CV curves, it can be qualitatively discerned that the **UF-Ca-900-3:1** sample has the largest specific capacitance while those of **UF-Ca-700-3:1** and **UF-Ca-800-3:1** samples are much lower and almost the same in areas. The incline of the CV curves in Fig. 6a reveals that a resistive component, mainly due to a hindered mobility of ions in micropores and/or a low electrical conductivity of the electrode, is involved in the charging process. The impact of resistive component becomes smaller as the activation temperature increases [32]. Hence, the **UF-Ca-900-3:1** sample shows the lowest resistance and the highest capacitance, compared with the other samples, which certainly relative with its highest values of S_{BET} (*ca.* 1009 m^2 g^{-1}) and V_T (*ca.* 0.79 cm^3 g^{-1}), as displayed in Table 2.

When further increasing the scan rates to 50/100/200 mV s^{-1}, the CV curve of the **UF-Ca-900-3:1** sample can retain the approximately rectangular behavior whilst those of **UF-Ca-700-3:1** and **UF-Ca-800-3:1** samples become more distorted in shape, as shown in Fig. 6b–d. As was reported, the CV curve shape and the specific capacitance for activated carbon-based electrodes can significantly degrade as the voltage scan rate is increased [33]. Nevertheless, the **UF-Ca-900-3:1** sample in present work can exhibit excellent CV behavior at wide scan rates from 20 to 200 mV s^{-1}, always showing approximately rectangular shape. For small potential scan rates, electrolytes have adequate time to enter into micropores, and micropores were effectively used for forming double-layer capacitance [34]. Another possible reason for the insensitivity to varying voltage scan rates is a short and equal diffusion path length of the ions in the electrolyte [35].

Table 2
Characteristic surface areas and pore structures of the carbon samples.

Sample	BET surface area (m^2 g^{-1})			Langmuir surface area (m^2 g^{-1})	Total pore volume (cm^3 g^{-1})	Micropore volume (cm^3 g^{-1})	Average pore width (nm)
	Total	S_{micro}	$S_{external}$				
UF-Ca-700-3:1	128	61	67	172	0.14	0.03	4.4
UF-Ca-800-3:1	441	280	161	588	0.35	0.13	3.2
UF-Ca-900-3:1	1009	471	538	1370	0.79	0.21	3.1

Notes: 1. S_{micro} represents the micropore area; 2. $S_{external}$ represents the external surface area.

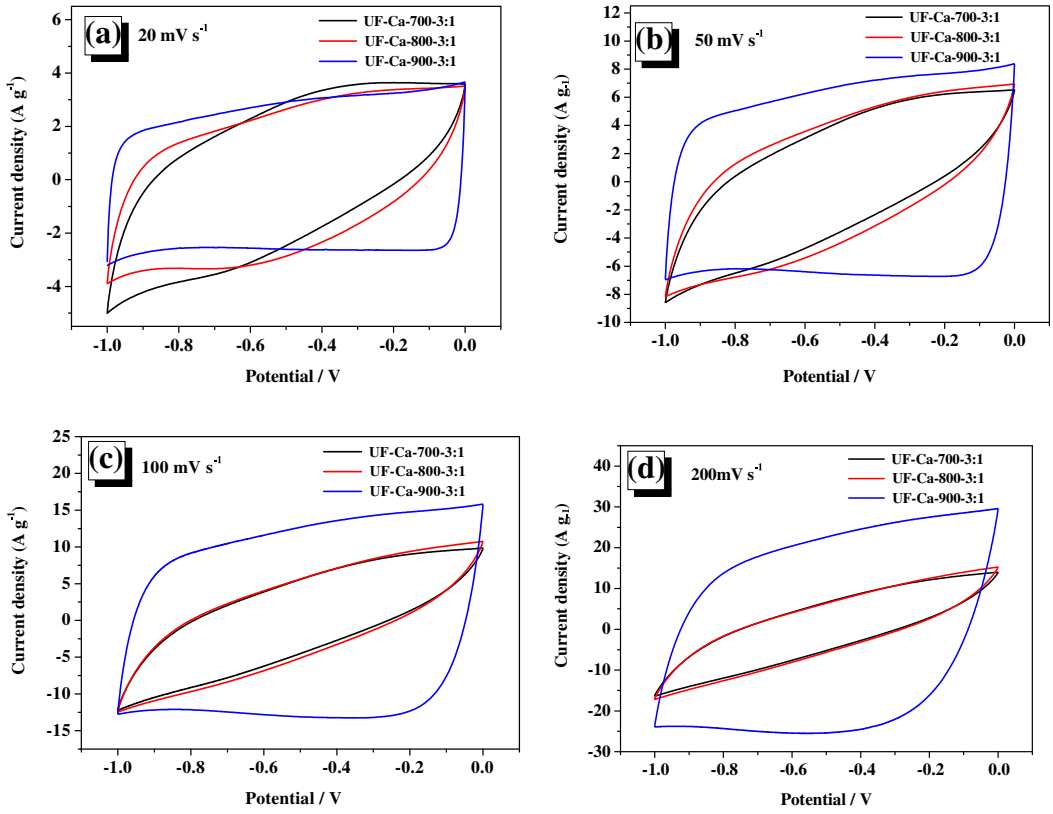

Fig. 6. Cyclic voltammograms of the **UF-Ca-700-3:1**, **UF-Ca-800-3:1** and (d) **UF-Ca-900-3:1** samples at various scan rates of (a) 20 mV s^{-1}, (b) 50 mV s^{-1}, (c) 100 mV s^{-1}, (d) 200 mV s^{-1}.

Given the excellent CV behaviors including shapes and areas (in Fig. 6) toward the **UF-Ca-900-3:1** sample, we specially investigated its CV curves at various scan rates ranging from 5 to 400 mV s^{-1}, as depicted in Fig. 7a. Apparently, along with the increase of scan rates, the CV curves nearly retain the rectangular shapes even at high scan rate of 400 mV s^{-1} Fig. 7b displays the galvanostatic charge–discharge curves measured at various current densities from 0.5 to 20 A g^{-1}, in which all curves exhibit favorable symmetry and linearity with almost constant slopes in a potential range of −1.0–0 V. Furthermore, increasing the current density can remarkably decrease the charge–discharge time because the electrolyte ions have sufficient time to enter and diffuse into the porosity at lower current densities [36]. That is to say, at the current density of 0.5 A g^{-1}, the **UF-Ca-900-3:1** sample exhibits the utmost charge–discharge time (*i.e.*, specific capacitance).

To comparatively study the capacitive performances of the present carbons, galvanostatic charge–discharge measurements designated at the current density of 10 A g^{-1} were conducted and the resultant profiles are given in Fig. 7c. It is clear to us that the **UF-Ca-900-3:1** sample possesses the optimal capacitive performance mainly owing to its large charge–discharge time and symmetric profile.

The specific capacitances of active electrode materials can be calculated according to the following equation:

$$C_m = \frac{I \times t}{\Delta V \times m}$$

where C_m (F g^{-1}) is the specific capacitance of the electrode based on the mass of active materials; I (A) is the discharge current; t (s) is the discharge time; ΔV (V) is the potential window (in present work, $\Delta V = 1.0$ V); and m (mg) is the mass of active materials loaded in working electrode.

Resultantly, specific capacitances of the present carbons at various current densities from 0.5 to 40 A g^{-1} are shown in Fig. 7d. In cases of the current densities as 0.5/1.0/2.0 A g^{-1}, the **UF-Ca-700-3:1** sample has relatively large specific capacitances (C_m, F g^{-1}) and the utmost one is of *ca.* 334.8 F g^{-1} at the current density of 0.5 A g^{-1}. The present performances are much better than the capacitive results previously reported [37], primarily owing to the incorporation of nitrogen species within porous carbons. However, the **UF-Ca-700-3:1**/**UF-Ca-800-3:1** sample's specific capacitances sharply decrease in cases of the current densities beyond 3.0 A g^{-1}. Contrarily, the **UF-Ca-900-3:1** sample can possess high retention as *ca.* 67.1% and 51.4% at the high current densities of 20 and 40 A g^{-1}, respectively, clearly revealing its high rate capacity. To sum up, at low current densities from 0.5 to 2.0 A g^{-1}, the order of specific capacitance is as follows: **UF-Ca-700-3:1** > **UF-Ca-800-3:1** > **UF-Ca-900-3:1**, proportional to their nitrogen contents in carbons. However, specific capacitances of the **UF-Ca-700-3:1**/**UF-Ca-800-3:1** samples decrease sharply mostly due to their low specific surface area and total pore volume.

Long cycle life is a crucial parameter for supercapacitors electrode materials [38,39]. Fig. 7e presents the specific capacitance of the **UF-Ca-900-3:1** sample as a function of cycle number. Interestingly, it exhibits a very a stable capacitance (~99.22% of the original capacitance) after 5000 cycles of charging and discharging, indeed indicating its long-term electrochemical stability. The galvanostatic charge–discharge curves of the 1st and 5000th cycle toward the **UF-Ca-900-3:1** sample at the current density of 10 A g^{-1} are shown in Fig. 7f. In particular, the inset of Fig. 7f reveals that IR drop (*i.e.* potential drop) of the 1st cycle is much lower than that of

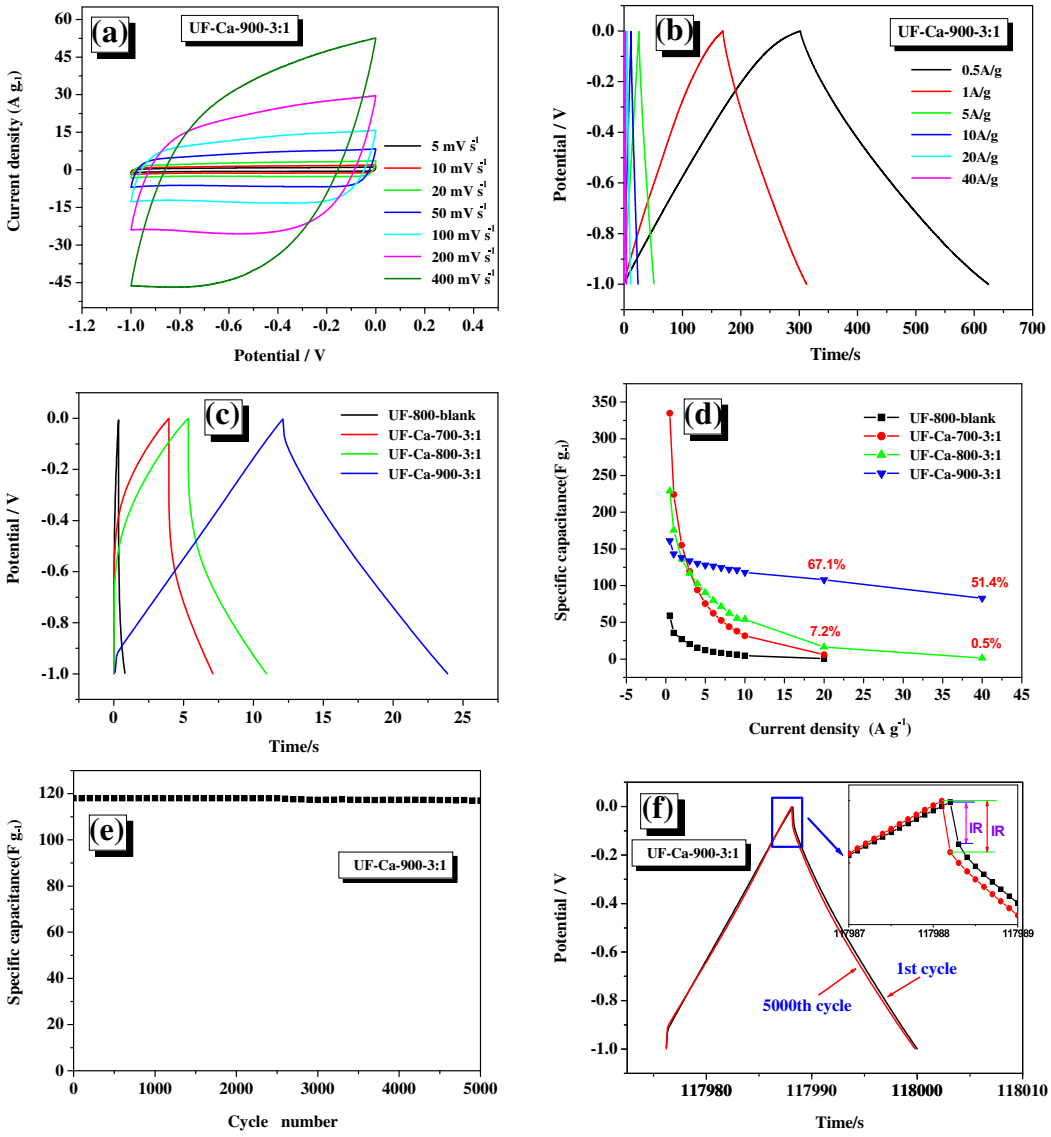

Fig. 7. (a) Cyclic voltammograms of the **UF-Ca-900-3:1** sample at various scan rates; (b) Galvanostatic charge–discharge curves measured at various current densities; (c) Galvanostatic charge–discharge curves measured at the current density of 10 A g^{-1}; (d) Specific capacitances at various current densities; (e) Cycling stability of the carbon samples; (f) Galvanostatic charge–discharge curves of the 1st and 5000th cycle toward the **UF-Ca-900-3:1** sample at the current density of 10 A g^{-1}.

the 5000th cycle at the very beginning of the discharge processes, in which the IR drop is caused by the overall internal resistance of the electrode [40].

Ragone plot is commonly utilized to illustrate the energy density (the storage capacity) as a function of power density (the rate of charge/discharge) of the electrode materials, which can be calculated according to the equations as follows:

$$E = \frac{1}{2}CV^2$$

$$P = \frac{E}{t}$$

where E (Wh kg^{-1}) is the average energy density; C (F g^{-1}) is the specific capacitance; V (V) is the potential window; P (W kg^{-1}) is the average power density and t (s) is the discharge time.

Fig. 8a indicates the overall Ragone plots of the present carbon samples, in which the **UF-Ca-900-3:1** sample exhibits the mostly acceptable performance. More precisely, it has a high energy density of *ca.* 22.4 Wh kg^{-1} at a power density of *ca.* 0.25 kW kg^{-1}, and a high power density of *ca.* 20 kW kg^{-1} at an energy density of *ca.* 11.5 Wh kg^{-1}. The present values for energy densities are much higher than those of commercial carbon supercapacitors usually as 4–5 Wh kg^{-1} [41], as well as the Partnership for a New Generation of Vehicles (PNGV) power target (namely, 15 kW kg^{-1}) [42].

Nyquist plot, also known as electrochemical impedance spectroscopy (EIS), shows the frequency response of the electrode/electrolyte system and is a plot of the imaginary component of the impedance against the real component. The Nyquist plots toward the present carbons were measured before and after 100 cycles and further fitted by ZView software, as indicated in Fig. 8b–c. Each Nyquist plot basically consists of a depressed semicircle in the high frequency region and a straight line in the low frequency region. In details, the semicircle associates with the surface properties of porous electrode and corresponds to the Faradic charge-transfer resistance [43]. The slope of the 45° portion, as dominated the Warburg resistance, is a result of the frequency dependence of ion diffusion/transport in the electrolyte [44]. Moreover, as depicted in

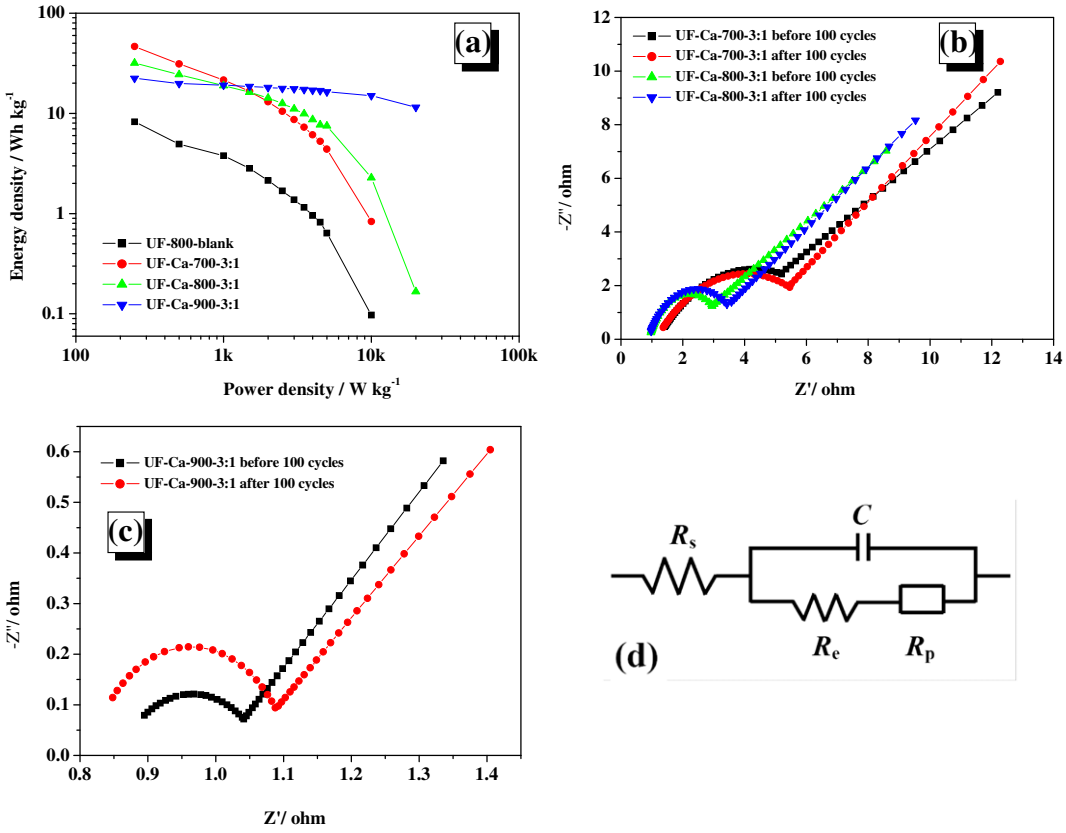

Fig. 8. (a) Ragone plots showing energy density *vs.* power density of the carbon samples; (b, c) Nyquist plots before/after 100 cycles of the carbon samples; (d) Equivalent circuit modeling.

Table 3
The overall resistance (R_t), electrical connection resistance (R_e), electrolyte resistance (R_s), and resistance of ion migration in carbon micropores (R_p) of the carbon samples.

Samples	Resistance (Ohm)			
	R_t	R_s	R_e	R_p
UF-Ca-700-3:1 before 100 cycles	12.197	1.416	3.785	6.996
UF-Ca-700-3:1 after 100 cycles	12.281	1.370	4.096	6.815
UF-Ca-800-3:1 before 100 cycles	8.584	0.970	1.961	5.653
UF-Ca-800-3:1 after 100 cycles	9.530	0.978	2.454	6.098
UF-Ca-900-3:1 before 100 cycles	1.336	0.895	0.147	0.294
UF-Ca-900-3:1 after 100 cycles	1.405	0.848	0.240	0.317

Fig. 8b–c, each semicircular arc after 100 charge–discharge cycles has slightly increased in size compared with that of the pristine one, primarily revealing the increase of the charge-transfer resistance [45]. The EIS can be fitted by an equivalent circuit (Fig. 8d) consisting of electrical connection resistance (R_e), electrolyte resistance (R_s) and resistance of ion migration in carbon micropores (R_p), as well as overall resistance (R_t), and the resultant values are summarized in Table 3.

4. Conclusions

In summary, a template synthetic method has been developed to prepare nitrogen-doped porous carbons, using UF resins as carbon source and $Ca(OAc)_2 \cdot H_2O$ as hard template. This approach has several advantages for the synthesis of the nitrogen-doped porous carbon: (1) UF resins can not only serve as carbon source but also as nitrogen source and the existence of nitrogen incorporated into carbons can benefit for the increase of capacitive performance for supercapacitors. (2) The residue such as $CaCO_3$, CaO and $Ca(OH)_2$ can be readily removed by dilute HCl solution at room temperature, which avoids the use of toxic reagents such as NaOH and HF for the etching of conventional silica templates. (3) The surface areas and pore structures of porous carbon were simply tuned by varying the mass ratios of UF resins-to-$Ca(OAc)_2 \cdot H_2O$ and carbonization temperatures. (4) The **UF-Ca-900-3:1** sample exhibits excellent long-term electrochemical stability within 5000 cycles. The nitrogen-doped carbon represents an alternative electrode material for supercapacitors, which can potentially be applied for large-scale industrial production.

Acknowledgments

This work was financially supported by the National Natural Science Foundation of China (21101052), China Postdoctoral Science Foundation (20100480045), and National Training Programs of Innovation and Entrepreneurship for Undergraduates (201210359033). Dr. Zhong Jie Zhang also thanks the financial support from Anhui Province Key Laboratory of Environment-friendly Polymer Materials, Anhui University, Hefei 230039, China (KF2012009). The authors gratefully thank the helpful discussion with Prof. Zheng Hua Wang at Anhui Normal University.

Appendix A. Supplementary material

Supplementary material related to this article can be found at http://dx.doi.org/10.1016/j.jpowsour.2012.12.054.

References

[1] L.L. Zhang, X.S. Zhao, Chem. Soc. Rev. 38 (2009) 2520–2531.
[2] P. Simon, Y. Gogotsi, Nat. Mater. 7 (2008) 845–854.
[3] Y.W. Zhu, S. Murali, M.D. Stoller, K.J. Ganesh, W.W. Cai, P.J. Ferreira, A. Pirkle, R.M. Wallace, K.A. Cychosz, M. Thommes, D. Su, E.A. Stach, R.S. Ruoff, Science 332 (2011) 1537–1541.
[4] M.D. Stoller, R.S. Ruoff, Energy Environ. Sci. 3 (2010) 1294–1301.
[5] A.G. Pandolfo, A.E. Hollenkamp, J. Power Sources 157 (2006) 11–27.
[6] J. Chmiola, G. Yushin, Y. Gogotsi, C. Portet, P. Simon, P.L. Taberna, Science 313 (2006) 1760–1763.
[7] J.S. Huang, B.G. Sumpter, V. Meunier, Angew. Chem. Int. Ed. 47 (2008) 520–524.
[8] J.H. Knox, B. Kaur, G.R. Millward, J. Chromatogr. 352 (1986) 3–25.
[9] J.W. Lee, J.Y. Kim, T.H. Hyeon, Adv. Mater. 18 (2006) 2073–2094.
[10] Y.P. Zhai, Y.Q. Dou, D.Y. Zhao, P.F. Fulvio, R.T. Mayes, S. Dai, Adv. Mater. 23 (2011) 4828–4850.
[11] B. Liu, H. Shioyama, T. Akita, Q. Xu, J. Am. Chem. Soc. 130 (2008) 5390–5391.
[12] S. Alvarez, A.B. Fuertes, Carbon 42 (2004) 433–436.
[13] T. Kyotani, Z.X. Ma, A. Tomita, Carbon 41 (2003) 1451–1459.
[14] T. Morishita, T. Tsumura, M. Toyoda, J. Przepiórski, A.W. Morawski, H. Konno, M. Inagaki, Carbon 48 (2010) 2690–2707.
[15] D.W. Wang, F. Li, L.C. Yin, X. Lu, Z.G. Chen, I.R. Gentle, G.Q. Lu, H.M. Cheng, Chem. Eur. J. 18 (2012) 5345–5351.
[16] M.G. Hahm, A.L.M. Reddy, D.P. Cole, M. Rivera, J.A. Vento, J. Nam, H.Y. Jung, Y.L. Kim, N.T. Narayanan, D.P. Hashim, C. Galande, Y.J. Jung, M. Bundy, S. Karna, P.M. Ajayan, R. Vajtai, Nano Lett. 12 (2012) 5616–5621.
[17] L.F. Chen, X.D. Zhang, H.W. Liang, M.G. Kong, Q.F. Guan, P. Chen, Z.Y. Wu, S.H. Yu, ACS Nano 6 (2012) 7092–7102.
[18] D. Asmi, I.M. Low, Ceramics Int. 34 (2008) 311–316.
[19] T.J. Schwartz, A.R.P. van Heiningen, M.C. Wheeler, Green Chem. 12 (2010) 1353–1356.
[20] T. Yin, M.Z. Rong, M.Q. Zhang, G.C. Yang, Compos. Sci. Technol. 67 (2007) 201–212.
[21] T.I.T. Okpalugo, P. Papakonstantinou, H. Murphy, J. McLaughlin, N.M.D. Brown, Carbon 43 (2005) 153–161.
[22] C. Pevida, T.C. Drage, C.E. Snape, Carbon 46 (2008) 1464–1474.
[23] J.R. Pels, F. Kapteijn, J.A. Moulijn, Q. Zhu, K.M. Thomas, Carbon 33 (1995) 1641–1653.
[24] T. Horikawa, N. Sakao, T. Sekida, J. Hayashi, D.D. Do, M. Katoh, Carbon 50 (2012) 1833.
[25] H. Liu, Y. Zhang, R.Y. Li, X.L. Sun, S. Désilets, H. Abou-Rachid, M. Jaidann, L.S. Lussier, Carbon 48 (2010) 1498–1507.
[26] K.S.W. Sing, Carbon 32 (1994) 1311–1317.
[27] C. Sangwichien, G.L. Aranovich, M.D. Donohue, Colloids Surf. A 206 (2002) 313–320.
[28] W. Xing, C.C. Huang, S.P. Zhuo, X. Yuan, G.Q. Wang, D. Hulicova-Jurcakova, Z.F. Yan, G.Q. Lu, Carbon 47 (2009) 1715–1722.
[29] E. Frackowiak, F. Béguin, Carbon 39 (2001) 937–950.
[30] C.S. Du, N. Pan, Nanotechnology 17 (2006) 5314–5318.
[31] M. Seredych, D.H. Jurcakova, G.Q. Lu, T.J. Bandosz, Carbon 46 (2008) 1475–1488.
[32] B.H. Kim, N.N. Bui, K.S. Yang, M.E. Cruz, J.P. Ferraris, Bull. Korean Chem. Soc. 30 (2009) 1967–1972.
[33] G. Lota, T.A. Centeno, E. Frackowiak, F. Stoechli, Electrochim. Acta 53 (2008) 2210–2216.
[34] X.L. Li, C.L. Han, X.Y. Chen, C.W. Shi, Micropor. Mesopor. Mater. 131 (2010) 303–309.
[35] M.D. Stoller, S. Park, Y.W. Zhu, J. An, R.S. Ruoff, Nano Lett. 8 (2008) 3498–3502.
[36] Q. Cheng, J. Tang, J. Ma, H. Zhang, N. Shinya, L.C. Qin, Phys. Chem. Chem. Phys. 13 (2011) 17615–17624.
[37] H. Nishihara, T. Kyotani, Adv. Mater. 24 (2012) 4473–4498.
[38] T. Brousse, P.L. Taberna, O. Crosnier, R. Dugas, P. Guillemet, Y. Scudeller, Y.K. Zhou, F. Favier, D. Bélanger, P. Simon, J. Power Sources 173 (2007) 633–641.
[39] C. Guan, X.H. Xia, N. Meng, Z.Y. Zeng, X.H. Cao, C. Soci, H. Zhang, H.J. Fan, Energy Environ. Sci. 5 (2012) 9085–9090.
[40] L. Zhang, G.Q. Shi, J. Phys. Chem. C 115 (2011) 17206–17212.
[41] A. Burke, Electrochim. Acta 53 (2007) 1083–1091.
[42] D.W. Wang, F. Li, M. Liu, G.Q. Lu, H.M. Cheng, Angew. Chem. Int. Ed. 47 (2008) 373–376.
[43] J.W. Lang, L.B. Kong, W.J. Wu, Y.C. Luo, L. Kang, Chem. Commun. (2008) 4213–4215.
[44] W.F. Wei, X.W. Cui, W.X. Chen, D.G. Ivey, Electrochim. Acta 54 (2009) 2271–2275.
[45] B.Z. Fang, J.H. Kim, M.S. Kim, A. Bonakdarpour, A. Lam, D.P. Wilkinson, J.S. Yu, J. Mater. Chem. 22 (2012) 19031–19038.